

# Indirect Optimization of Three-Dimensional Finite-Burning Interplanetary Transfers Including Spiral Dynamics

Christopher L. Ranieri\* and Cesar A. Ocampo†  
University of Texas at Austin, Austin, Texas 78712

DOI: 10.2514/1.38170

The indirect optimization problem for a three-dimensional transfer from low Earth orbit to low Mars orbit is solved. A step-by-step process developed for a two-dimensional model and techniques for accurately estimating the unknown costates for three-dimensional escape and capture spirals are used. Minimum-propellant trajectories for finite-burning engines are calculated. Solutions are considered with and without control limits on specific impulse and compared with previous research. Unlike other research, the entire trajectory, including the Martian capture sequence, is integrated in an Earth-referenced frame. Additionally, the capture sequence is not found by iteratively lowering the final targeted low Mars orbit, but the desired final orbit is directly targeted with no successive iterations of increasingly smaller low Mars orbits. As in the two-dimensional case, more fuel-efficient trajectories are found for the same mission objectives and constraints published in other research, emphasizing the importance of this technique. Whereas previous research only achieved final Martian orbits of 6 Mars radii  $DU_M$  (20,382 km), the new approach finds solutions for final Martian circular orbits of 1.47–2.00  $DU_M$  (5000–6794 km).

## Nomenclature

<b>A</b>	=	rotation matrix from the heliocentric equatorial frame to the Earth-centered rotating frame in three dimensions	<b>EQECM</b>	=	rotation from the heliocentric equatorial to the Martian ecliptic frame in three dimensions
$A', B', C'$	=	auxiliary variables used to express the areocentric spacecraft position in the Earth-centered rotating coordinates	$\mathbf{e}_*$	=	unit vector for coordinate frames
<b>AB</b>	=	rotation matrix from the Mars-centered rotating frame to the Earth-centered rotating frame in three dimensions	$G$	=	Bolza function
<b>ABd</b>	=	time derivative of <b>AB</b>	$H$	=	Hamiltonian
$a$	=	thrust-acceleration magnitude	$J$	=	cost function
<b>B</b>	=	rotation matrix from the Mars-centered rotating frame to heliocentric equatorial frame in three dimensions	<b>MCR</b>	=	spacecraft-centered spherical frame rotating with Mars around the sun
<b>ECR</b>	=	spacecraft-centered spherical frame rotating with Earth around the sun	<b>MCR2RM</b>	=	rotation from the Mars-centered rotating frame to the Mars planetary spherical frame in three dimensions
<b>EC2ECR</b>	=	rotation matrix from the Earth ecliptic frame to the Earth-centered rotating frame in three dimensions	<b>MCR2EC</b>	=	rotation from the Mars-centered rotating frame to the Mars ecliptic frame in three dimensions
<b>EC2EQ</b>	=	rotation from the Earth ecliptic frame to the heliocentric equatorial frame in three dimensions	$m$	=	spacecraft mass
<b>EC2EQM</b>	=	rotation from the Martian ecliptic frame to the heliocentric equatorial frame in three dimensions	$P$	=	spacecraft power
<b>EC2RE</b>	=	rotation from the Earth ecliptic frame to the Earth planetary spherical frame in three dimensions	$\mathbf{R}_s$	=	position vector of the spacecraft from the sun
<b>EQEC</b>	=	rotation from the heliocentric equatorial to the Earth ecliptic frame in three dimensions	$\mathbf{R}_*$	=	position vector of planet * from the sun
			<b>RE2ECR</b>	=	rotation from the Earth planetary spherical to the Earth-centered rotating frame in three dimensions
			<b>RM2MEC</b>	=	rotation from the Martian planetary spherical to the Martian ecliptic frame in three dimensions
			$r, \theta, \Phi$	=	spherical position components
			$\mathbf{r}$	=	position vector in the Earth-centered rotating frame
			$r_r, r_\theta, r_\Phi$	=	position of the spacecraft ( $\mathbf{r}$ ) with respect to Earth in the Earth planetary spherical frame
			$t$	=	time
			$\mathbf{u}$	=	thrust-acceleration unit direction vector
			$V_{RS}, V_{\theta S}, V_{\Phi S}$	=	inertial heliocentric velocity components ( $S$ subscript) of the spacecraft in the Earth-centered rotating frame ( $R, \theta$ , and $\Phi$ subscripts) axes
			$V_r, V_\theta, V_\Phi$	=	spherical velocity components of the spacecraft in the Earth-centered and Mars-centered rotating frames
			$V_{*r}, V_{*\theta}$	=	polar velocity components of planet * around the sun
			$\lambda$	=	costates
			$\mu$	=	gravitational parameter
			$\omega$	=	costate vector adjoined to constraints/targets in the Bolza function

Presented as Paper AAS 07-207 at the AAS/AIAA Spaceflight Mechanics Meeting, Sedona, AZ, 28–31 January 2007; received 22 April 2008; revision received 7 September 2008; accepted for publication 21 September 2008. Copyright © 2008 by the American Institute of Aeronautics and Astronautics, Inc. All rights reserved. Copies of this paper may be made for personal or internal use, on condition that the copier pay the \$10.00 per-copy fee to the Copyright Clearance Center, Inc., 222 Rosewood Drive, Danvers, MA 01923; include the code 0731-5090/09 \$10.00 in correspondence with the CCC.

\*National Science Foundation Research Graduate Student, Department of Aerospace Engineering and Engineering Mechanics, 1 University Station, Mail Stop C0600; chris.ranieri@gmail.com. Member AIAA.

†Associate Professor, Department of Aerospace Engineering and Engineering Mechanics, 1 University Station, Mail Stop C0600; cesar.ocampo@mail.utexas.edu. Member AIAA.

## Subscripts

$E$	=	Earth
$EC$	=	ecliptic heliocentric inertial frame
$M$	=	Mars
$*$	=	axis or planet under discussion

## Superscript

$'$	=	indicates that a variable is measured with respect to the Mars-centered rotating frame, not the Earth-centered rotating frame
-----	---	---

## Introduction

**A**N INDIRECT optimization procedure is presented for optimizing the fuel usage for transfers for finite-burning engines from low Earth orbit (LEO) to low Martian orbit (LMO). The engine model used is a variable-specific-impulse (VSI) engine in which the power is constant but the specific impulse  $I_{sp}$  or thrust magnitude can be throttled accordingly. Examples are also presented in which control limits are introduced for the  $I_{sp}$  in particular cases in which the  $I_{sp}$  is constrained to be a constant during the escape. The overall trajectory can be categorized by three sections: Earth escape spiral, heliocentric transfer leg, and Mars capture spiral. Analysis and derivation of the optimality conditions for the heliocentric legs, particularly for time-constrained round-trip missions, have previously been developed [1,2]. Additionally, in-depth analysis has been performed focusing solely on the escape and capture portions of such missions [3]. Using those works, for the two-dimensional simplification of the Earth–Mars system, a step-by-step process was developed that facilitated finding optimal interplanetary missions with better fuel efficiency and more involved capture sequences at Mars than published previously [4]. That process is expanded here for a more realistic three-dimensional system.

The research presented here focuses on indirect optimization and aims to use no analytical simplifications to the problem dynamics. Other works have analyzed end-to-end LEO-to-LMO [5,6] or low-lunar-orbit (LLO) [7–10] missions using indirect methods. However, these works may simplify the engine dynamics, particularly during the most detailed and complicated phases of the trajectories, the spirals, by limiting the thrust to be constant [7–9] or, at the very least, using a constant-thrust spiral as the first guess [5,6]. This paper will show the importance of the first guess in determining which local optimal solution is generated with respect to the global solution space. Other approaches just use a patched conic approach and calculate the spirals and heliocentric legs independently. These works do not even optimize the spirals themselves, but rather calculate fixed constant-thrust spirals, with the thrust fixed along the velocity vector until the spacecraft achieves escape [11,12].

As in past research [5,6], a series of subproblems must be optimized to construct the full mission. The full mission includes gravitational effects during the entire trajectory from all three major bodies of the problem: Earth, sun, and Mars. The final examples extend past three-dimensional results [6] by including the effects of lunar gravity on the trajectory. The main difference of the new approach is to analyze the entire trajectory in an Earth-referenced spherical coordinate system rotating with Earth (labeled as ECR) as the Earth revolves around the sun. To facilitate this approach, a transformation is derived to convert costates in a Mars-referenced spherical frame rotating with Mars (labeled as MCR) as Mars revolves around the sun to their equivalent costates in the ECR frame. This greatly simplifies the optimal control conditions that must be satisfied at the patch point. Additionally, the problem is formulated as a multiple-shooting problem in which the Earth escape and Martian capture sequences are iterated on separately, which is in contrast to the single-shooting method used previously [5,6].

Results are presented for cases with zero-inclination escape and capture spirals as well as for inclined capture spirals. The results present scenarios for both cases for missions that exactly replicate published benchmarks (with improved performance) as well as

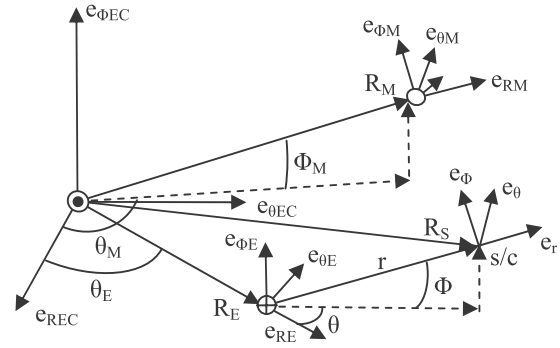


**Fig. 1** Spherical coordinate systems referenced to the Earth ecliptic frame.

solutions that involve significantly more complicated capture sequences that push the numerical limits of the method. Additionally, solutions are presented that include a fourth-body perturbation from the moon, showing the effects of closer lunar approaches during the escape.

## Equations of Motion

Noninertial coordinate frames (ECR and MCR) that track the motion of the planets with respect to the sun are used. These coordinate systems can be seen in Fig. 1, which depicts three spherical coordinate systems referenced to a heliocentric inertial frame ( $e_{REC}$ ,  $e_{\theta EC}$ ,  $e_{\phi EC}$ ) that is aligned with the Earth ecliptic frame: Earth spherical ( $e_{RE}$ ,  $e_{\theta E}$ , and  $e_{\phi E}$ ), Mars spherical ( $e_{RM}$ ,  $e_{\theta M}$ , and  $e_{\phi M}$ ), and the spacecraft-centered Earth-position-referenced frame (ECR  $e_r$ ,  $e_\theta$ , and  $e_\phi$ ). The Jet Propulsion Laboratory (JPL) DE405 ephemeris is used at the epoch to determine the heliocentric<sup>‡</sup> positions of Earth and Mars and then the planets are integrated numerically using two-body dynamics under the influence of the sun [6]. Therefore, the Earth will only move in two dimensions in the  $e_{REC}$ ,  $e_{\theta EC}$  plane. These simplifications allow the equations of motion to be written more succinctly than if the ephemeris is used for the time history of the planets. For the time scales examined in this paper ( $\sim 1$  year), the differences are not very significant. When capture spirals are calculated in an MCR frame, the heliocentric inertial frame is aligned with the Mars ecliptic frame, which is defined by the two-body orbit of Mars around the sun. Any component of the spacecraft state that is measured with respect to Mars will be denoted with a prime on the variable, such as  $r'$ . The planets and sun are denoted with their astrological symbols in Fig. 1.

Using the ECR coordinate system, the state and state time derivative are defined:

$$\mathbf{x} = \begin{bmatrix} r \\ \theta \\ \phi \\ v_r \\ v_\theta \\ v_\phi \end{bmatrix} \quad (1)$$

$$\dot{r} = v_r \quad (2)$$

$$\dot{\theta} = v_\theta / r \cos \phi \quad (3)$$

$$\dot{\phi} = v_\phi / r \quad (4)$$

<sup>‡</sup>Data available at <http://ssd.jpl.nasa.gov/?ephemerides> [retrieved 3 November 2008].

$$\begin{aligned}\dot{v}_r = & (v_\theta^2 + v_\phi^2)/r + 2v_\theta\dot{\theta}_E \cos \phi + r(\dot{\theta}_E \cos \phi)^2 \\ & + R_E\dot{\theta}_E^2 \cos \phi \cos \theta - \ddot{R}_E \cos \phi \cos \theta \\ & - (R_E\ddot{\theta}_E + 2\dot{R}_E\dot{\theta}_E) \cos \phi \sin \theta - \mu_E/r^2 \\ & - \mu_S R_{Sr}/R_S^3 - \mu_M r'_r/r^3 + au_r\end{aligned}\quad (5)$$

$$\begin{aligned}\dot{v}_\theta = & -v_r v_\theta/r + 2\dot{\theta}_E(v_\phi \sin \phi - v_r \cos \phi) - r\ddot{\theta}_E \cos \phi \\ & + v_\phi v_\theta \tan \phi/r - R_E\ddot{\theta}_E - 2\dot{R}_E\dot{\theta}_E \cos \theta + \ddot{R}_E \sin \theta \\ & - R_E\dot{\theta}_E^2 \sin \theta - \mu_S R_{S\theta}/R_S^3 - \mu_M r'_\theta/r^3 + au_\theta\end{aligned}\quad (6)$$

$$\begin{aligned}\dot{v}_\phi = & -v_r v_\phi/r - v_\theta^2 \tan \phi/r - 2v_\theta\dot{\theta}_E \sin \phi + \ddot{R}_E \sin \phi \cos \theta \\ & - \dot{\theta}_E^2 \sin \phi (r \cos \phi + R_E \cos \theta) + R_E\ddot{\theta}_E \sin \phi \sin \theta \\ & + 2\dot{R}_E\dot{\theta}_E \sin \phi \sin \theta - \mu_S R_{S\phi}/R_S^3 - \mu_M r'_\phi/r^3 + au_\phi\end{aligned}\quad (7)$$

The second time derivatives of the polar position of Earth were derived previously [4]:

$$\ddot{R}_E = -\mu_S/R_S^3 + v_{\theta E}^2/R_E \quad (8)$$

$$\ddot{\theta}_E = -2\dot{R}_E V_{\theta E}/R_E^2 \quad (9)$$

The heliocentric spacecraft position in the ECR coordinates is

$$\mathbf{R}_S = \mathbf{r} + \mathbf{R}_E = \begin{bmatrix} R_{Sr} \\ R_{S\theta} \\ R_{S\phi} \end{bmatrix} = \begin{bmatrix} r + R_E \cos \phi \cos \theta \\ -R_E \sin \theta \\ -R_E \sin \phi \cos \theta \end{bmatrix}_{(e_r, e_\theta, e_\phi)} \quad (10)$$

$$R_S = [r^2 + 2rR_E \cos \phi \cos \theta + R_E^2]^{1/2} \quad (11)$$

The areocentric spacecraft position in the ECR coordinates is

$$\mathbf{r}' = \begin{bmatrix} r'_r \\ r'_\theta \\ r'_\phi \end{bmatrix} = \begin{bmatrix} r + R_E \cos \phi \cos \theta - R_{MA'} \\ -R_E \sin \theta - R_{MB'} \\ -R_E \sin \phi \cos \theta - R_{MC'} \end{bmatrix}_{(e_r, e_\theta, e_\phi)} \quad (12)$$

$$\begin{bmatrix} A' \\ B' \\ C' \end{bmatrix} = \begin{bmatrix} \cos \phi_M \cos \phi \cos(\theta + \theta_E - \theta_M) + \sin \phi_M \sin \phi \\ -\cos \phi_M \sin(\theta + \theta_E - \theta_M) \\ \sin \phi_M \cos \phi - \cos \phi_M \sin \phi \cos(\theta + \theta_E - \theta_M) \end{bmatrix} \quad (13)$$

$$\begin{aligned}r' = & [r^2 + 2rR_E \cos \phi \cos \theta + R_M^2 + R_E^2 - 2rR_{MA'} \\ & - 2R_E R_{MB'} \cos \phi \cos(\theta_E - \theta_M)]^{1/2}\end{aligned}\quad (14)$$

The equivalent equations can be determined in the MCR frame with a few modifications. It is important to note that the preceding defined equations of motion are not for a MCR frame referenced to the Mars spherical frame ( $e_{rM}$ ,  $e_{\theta M}$ , and  $e_{\phi M}$ ) seen in Fig. 1, which is referenced to the Earth ecliptic. To use the MCR equivalent equations, the planets' states must be written with respect to the Mars ecliptic frame rather than to the Earth ecliptic frame. In this frame, Mars moves in a two-dimensional, two-body orbit in the Martian ecliptic and Earth moves in three dimensions with respect to this Martian ecliptic plane. This is in contrast to the preceding ECR formulation in which Mars moves in three dimensions, both above and below the Earth ecliptic with the Earth's motion planar, as depicted in Fig. 1.

#### Optimal Control Problem

To minimize the spacecraft propellant for a VSI engine, it is possible to decouple the actual spacecraft mass and power from the

problem, and a formulation for the minimum-fuel problem can be used based solely on the accumulated thrust acceleration [13]:

$$\frac{1}{m_f} - \frac{1}{m_0} = \frac{1}{2} \int_{t_0}^{t_f} \left( \frac{a^2}{P} \right) dt \quad (15)$$

The optimal value for the power for an unconstrained VSI engine is a constant at the maximum power level. Using optimal control theory, a boundary-value problem is formed that, when satisfied, meets all of the first-order conditions for optimality [14]. Because the problem is formulated as a maximization problem, the cost function used is

$$J = \max \left[ -\frac{1}{2} \int_{t_0}^{t_f} a^2 dt \right] \quad (16)$$

Once the boundary-value problem has been solved to optimize the cost function laid out in Eq. (16), the final mass  $m_f$  in Eq. (15) can be found by specifying values for the vehicle power and initial mass value:

$$m_f = m_0 P_{\max} / (P_{\max} + J m_0) \quad (17)$$

All physical constraints of the optimization problem, such as the targeted state vector of the spacecraft at the final time at Mars, are adjoined to the cost function via the Bolza function  $G$  [14]:

$$J' = G - \frac{1}{2} \int_{t_0}^{t_f} a^2 dt \quad (18)$$

The controls are the thrust-acceleration magnitude  $a$  and its unit direction vector  $\mathbf{u}$ . Their optimal values are derived by maximizing the Hamiltonian with respect to the controls. The acceleration is aligned with the primer vector [15]:

$$H = \lambda^T \dot{\mathbf{x}} - a^2/2 \quad (19)$$

$$u_r^2 + u_\theta^2 + u_\phi^2 = 1 \quad (20)$$

$$\mathbf{u} = \lambda_v / \lambda_v \quad (21)$$

$$a = \lambda_v \quad (22)$$

Using the definition of the Hamiltonian, the costate equations can be found:

$$\dot{\lambda} = -H_x^T \quad (23)$$

The partial derivatives necessary to complete Eq. (23) are not defined here but can be found in more detail in other works [16]. If bounds on the  $I_{sp}$  are considered, a different cost function should be used:

$$J = \max(m_f) \quad (24)$$

As derived previously [3], a first guess for a solution with  $I_{sp}$  bounds can be found by multiplying the costates for the converged unconstrained problem of Eq. (16) by the scalar  $(m^2/P_{\max})$ .

#### Subproblems for End-to-End Optimization

The step-by-step process shown in Fig. 2 was developed to solve the LEO-to-LMO missions. Steps 1a–3a are identical to steps 1b–3b, except the  $a$  steps involve forward (FWD) integration from the initial conditions in an Earth-referenced frame, and the  $b$  steps involve backward (BWD) integration from the final targeted state in a Mars-referenced frame. A detailed explanation of each step and their differences with previous approaches to solving the indirect optimization of the LEO-LMO transfer can be found with the research on the two-dimensional problem [4]. The process is

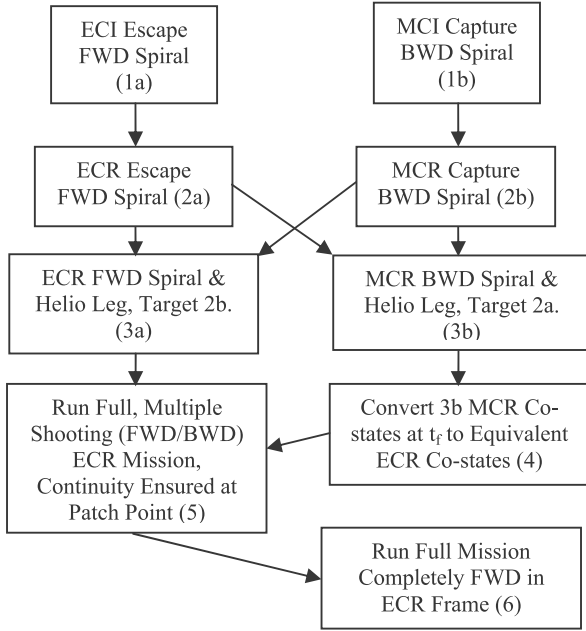


Fig. 2 Flowchart for subproblems for end-to-end optimization.

summarized here with discussion of important differences for the expansion to three dimensions.

#### Steps 1a and 1b

The goal of the first subproblem is to find fuel-optimal escape and capture spirals in an Earth-centered-inertial (ECI) coordinate system for the escape spirals or a Mars-centered-inertial (MCI) coordinate system for the capture spirals. These spirals terminate when the spacecraft has zero energy with respect to the spiral planet. Techniques have been developed to quickly and accurately estimate the unknown costates for two-dimensional escape and capture spirals, and this technique was used in the two-dimensional LEO–LMO research [3,4]. However, for the three-dimensional problem, the desired initial or final orbits may not be coplanar with the Earth ecliptic or Mars ecliptic frames and may therefore span three dimensions during the spiral periods. For these inclined cases, the transformation [3] is used that converts the converged costates for a two-dimensional spiral into the equivalent costates’ planar-inclined three-dimensional spiral.

#### Steps 2a and 2b

Although the solutions for the spirals in step 1 do not include the gravity of other bodies such as the sun and Mars/Earth and are performed in an inertial frame, the third-body perturbations and effects of the rotation of the ECR or MCR frames do not significantly alter the trajectory or the optimal costates for the escape or capture spirals of step 1. Therefore, the costates found in step 1 are the initial guess for spirals in the ECR or MCR frames.

#### Steps 3a and 3b

The goal of step 3 is to optimally transfer from LEO through an escape spiral, transition to heliocentric space, and target the capture point of the capture spiral found in step 2b. It was found that integrating both the Earth escape and the heliocentric transfer in the ECR frame is easier numerically and avoids the explicit formulation of the costates for the heliocentric transfer. For step 3b, the trajectory is integrated solely in the MCR frame and targets the escape point found in step 2a.

#### Step 4

This step is the most vital step of the process. After step 3a, there are two ways to solve the full mission. The first way, used in previous

works [5,6], integrates the capture forward and in the MCR frame, which is a single-shooting method. This can be difficult, as the final orbit must be iteratively lowered to the desired target orbit size when forming the capture spiral, and it encounters convergence limits at relatively large final orbits ( $6 DU_M$ ). Part of the numerical sensitivity is also associated with satisfying the conditions derived from the discontinuity at the patch point at which the state switches from the ECR to the MCR coordinates. These difficulties can be avoided. Incorporating the backward capture spiral and heliocentric leg from step 3b that targets the Earth escape point removes the need to iteratively lower the final orbit to form the capture spiral. This generates more involved capture sequences that terminate lower and have more revolutions around Mars. Using the backward spiral is accomplished with a transformation that converts the MCR costates of step 3b to their equivalent ECR costates. This allows the entire LEO-to-LMO mission to be integrated solely in the ECR frame with no state or costate discontinuities. It also forms a multiple-shooting method that allows both the Earth escape and the Mars capture to be directly modified by the boundary-value solver. This is in contrast to the previously used single-shooting method.

#### Earth Costates from the Martian Costates Transformation

This transformation is the key step for solving the two-dimensional LEO–LMO transfers [4] and is expanded here for the three-dimensional case. For a given transfer, the thrust magnitude in both the MCR and ECR frames must be identical and the thrust direction must point in the same inertial direction. Using this fact and the relationship between the velocity costates and thrust unit direction vector specified by Eqs. (21) and (22), the MCR velocity costates are converted to the ECR velocity costates. The MCR spacecraft state must be first converted to the equivalent ECR state vector. The rotation from the MCR frame to the Mars spherical frame (moves with Mars in Mars ecliptic) is defined:

$$\text{MCR 2RM} = \begin{bmatrix} \cos \phi' \cos \theta' & -\sin \theta' & -\sin \phi' \cos \theta' \\ \cos \phi' \sin \theta' & \cos \theta' & -\sin \phi' \sin \theta' \\ \sin \phi' & 0 & \cos \phi' \end{bmatrix} \quad (25)$$

The rotation that converts the Mars spherical frame to the Cartesian frame aligned with the Mars ecliptic is

$$\text{RM2MEC} = \begin{bmatrix} \cos \theta_M & -\sin \theta_M & 0 \\ \sin \theta_M & \cos \theta_M & 0 \\ 0 & 0 & 1 \end{bmatrix} \quad (26)$$

Together, these two rotations form the rotation that converts the MCR frame into the heliocentric inertial frame aligned with the Mars ecliptic (Mars perifocal frame).

$$\text{MCR 2EC} = (\text{RM2MEC})(\text{MCR2RM}) \quad (27)$$

The Cartesian position of the spacecraft in the Martian ecliptic frame is

$$\mathbf{R}_{S(iS,jS,kS)\text{MEC}} = (\text{MCR2EC})\mathbf{R}_{S(e'f',e\theta',e\phi')\text{MCR}} \quad (28)$$

The Cartesian heliocentric position of the spacecraft in the MCR frame basis is

$$\mathbf{R}_{S(\text{MCR})} = \mathbf{R}_M + \mathbf{r}' = \begin{bmatrix} R_{Sr} \\ R_{S\theta} \\ R_{S\phi} \end{bmatrix} = \begin{bmatrix} r' + R_M \cos \phi' \cos \theta' \\ -R_M \sin \theta' \\ -R_M \sin \phi' \cos \theta' \end{bmatrix}_{(e'_r, e'_\theta, e'_\phi)} \quad (29)$$

The Mars ecliptic frame is then rotated to the heliocentric equatorial frame using the three orbital angles that define the orbit of Mars around the sun:

$$\text{EQ2ECM} = \text{EC2EQM}^T = R_3(\omega')R_1(i')R_3(\Omega') \quad (30)$$

The Earth ecliptic frame is rotated from the heliocentric equatorial frame by

$$\mathbf{EQ2EC} = \mathbf{EC2EQ}^T = R_3(\omega)R_1(i)R_3(\Omega) \quad (31)$$

The spherical frame aligned with the Earth ( $e_{rE}$ ,  $e_{\theta E}$ , and  $e_{\phi E}$  in Fig. 1) is found by rotating from the Earth ecliptic frame using the following rotation:

$$\mathbf{EC2RE} = \begin{bmatrix} \cos \theta_E & \sin \theta_E & 0 \\ -\sin \theta_E & \cos \theta_E & 0 \\ 0 & 0 & 1 \end{bmatrix} \quad (32)$$

The position of the spacecraft from the sun in the Earth spherical frame rotated from the MCR frame is then defined as

$$\begin{aligned} \mathbf{R}_{S(eRE, e\theta E, e\phi E)} \\ = (\mathbf{EC2RE})(\mathbf{EQ2EC})(\mathbf{EC2EQM})(\mathbf{MCR2EC})\mathbf{R}_{S(er', e\theta', e\phi')} \mathbf{MCR} \end{aligned} \quad (33)$$

The position of the spacecraft from the Earth in the Earth spherical frame is

$$\mathbf{r}_{(eRE, e\theta E, e\phi E)} = \mathbf{R}_{S(eRE, e\theta E, e\phi E)} - \mathbf{R}_{E(eRE, e\theta E, e\phi E)} = \begin{bmatrix} r_r \\ r_\theta \\ r_\phi \end{bmatrix} \quad (34)$$

Using the position vector in the Earth spherical frame of Eq. (34), the spherical ECR state ( $r$ ,  $\theta$ , and  $\Phi$ ) can be recovered. The ECR frame ( $e_r$ ,  $e_\theta$ , and  $e_\phi$  in Fig. 1) is found by rotating from the Earth spherical frame ( $e_{rE}$ ,  $e_{\theta E}$ , and  $e_{\phi E}$  in Fig. 1) using the following rotation:

$$\mathbf{RE2ECR} = \begin{bmatrix} \cos \phi \cos \theta & \cos \phi \sin \theta & \sin \phi \\ -\sin \theta & \cos \theta & 0 \\ -\sin \phi \cos \theta & -\sin \phi \sin \theta & \cos \phi \end{bmatrix} \quad (35)$$

The ECR frame is then found from the Earth ecliptic using the following rotation:

$$\mathbf{EC2ECR} = \mathbf{RE2ECR} \times \mathbf{EC2RE} \quad (36)$$

The spacecraft velocity in the MCR frame can be converted into its equivalent ECR frame velocity by finding the inertial velocity of the spacecraft written in the MCR components by taking the time derivative of Eq. (29):

$$\begin{aligned} \dot{\mathbf{R}}_{S(er', e\theta', e\phi')} &= \begin{bmatrix} V_{RS'} \\ V_{\theta S'} \\ V_{\phi S'} \end{bmatrix} \\ &= \begin{bmatrix} v'_r + \dot{R}_M \cos \phi' \cos \theta' + R_M \dot{\theta}_M \cos \phi' \sin \theta' \\ v'_\theta - \dot{R}_M \sin \theta' + \dot{\theta}_M (r' \cos \phi' + R_M \cos \theta') \\ v'_\phi - \dot{R}_M \sin \phi' \cos \theta' - R_M \dot{\theta}_M \sin \phi' \sin \theta' \end{bmatrix}_{(er', e\theta', e\phi')} \end{aligned} \quad (37)$$

$$\dot{\mathbf{R}}_{S(er, e\theta, e\phi)} = \begin{bmatrix} V_{RS} \\ V_{\theta S} \\ V_{\phi S} \end{bmatrix} = (\mathbf{AB})\dot{\mathbf{R}}_{S(er', e\theta', e\phi')} \quad (38)$$

$$\mathbf{A} = \mathbf{EC2ECR} \times \mathbf{EQ2EC} \quad (39)$$

$$\mathbf{B} = \mathbf{EC2EQM} \times \mathbf{MCR2EC} \quad (40)$$

Taking the results of Eq. (38), the ECR velocity can be recovered by switching the terms in Eq. (37) to reflect the ECR state and rearranging for the ECR velocity vector ( $v_r$ ,  $v_\theta$ , and  $v_\phi$ ):

$$\begin{bmatrix} v_r \\ v_\theta \\ v_\phi \end{bmatrix} = \begin{bmatrix} V_{RS} - \dot{R}_E \cos \phi \cos \theta - R_E \dot{\theta}_E \cos \phi \sin \theta \\ V_{\theta S} + \dot{R}_E \sin \theta - \dot{\theta}_E (r \cos \phi + R_E \cos \theta) \\ V_{\phi S} + \dot{R}_E \sin \phi \cos \theta R_E + R_E \dot{\theta}_E \sin \phi \sin \theta \end{bmatrix}_{(er, e\theta, e\phi)} \quad (41)$$

Using Eqs. (34) and (41), the equivalent ECR state vector is converted from the original MCR state. In a similar fashion, the states of the planets in the ECR frame can be found from their MCR values. Because the velocity costate vector is aligned with the thrust direction, as seen in Eqs. (21) and (22), the MCR velocity costates can be rotated to their equivalent ECR values:

$$\lambda_v = (\mathbf{AB})\lambda'_v \quad (42)$$

The time derivative is taken from Eq. (42). The time derivative on the right-hand side is shown in Eq. (43), in which the costate derivatives are solved using the MCR equivalents of the costate equations. The terms on the left-hand side of Eq. (43) are just auxiliary variables:

$$\begin{bmatrix} \lambda_{vr} T \\ \lambda_{v\theta} T \\ \lambda_{v\phi} T \end{bmatrix} = \begin{bmatrix} ABd(1,1)\lambda'_{vr} + AB(1,1)\dot{\lambda}'_{vr} + ABd(1,2)\lambda'_{v\theta} + AB(1,2)\dot{\lambda}'_{v\theta} + ABd(1,3)\lambda'_{v\phi} + AB(1,3)\dot{\lambda}'_{v\phi} \\ ABd(2,1)\lambda'_{vr} + AB(2,1)\dot{\lambda}'_{vr} + ABd(2,2)\lambda'_{v\theta} + AB(2,2)\dot{\lambda}'_{v\theta} + ABd(2,3)\lambda'_{v\phi} + AB(2,3)\dot{\lambda}'_{v\phi} \\ ABd(3,1)\lambda'_{vr} + AB(3,1)\dot{\lambda}'_{vr} + ABd(3,2)\lambda'_{v\theta} + AB(3,2)\dot{\lambda}'_{v\theta} + ABd(3,3)\lambda'_{v\phi} + AB(3,3)\dot{\lambda}'_{v\phi} \end{bmatrix} \quad (43)$$

$$\frac{d\mathbf{AB}}{dt} = \mathbf{ABd} \quad (44)$$

Taking the time derivative of the left-hand side of Eq. (42), plugging in the appropriate terms from the costate equations (23), and rearranging for the ECR position costates yields

$$\begin{aligned} \begin{bmatrix} \lambda_r \\ \lambda_\theta \\ \lambda_\phi \end{bmatrix} &= \begin{bmatrix} -\lambda_{vr} T - \lambda_{vr} (\partial \dot{v}_r / \partial v_r) - \lambda_{v\theta} (\partial \dot{v}_\theta / \partial v_r) - \lambda_{v\phi} (\partial \dot{v}_\phi / \partial v_r) \\ r \cos \phi [-\lambda_{v\theta} T - \lambda_{vr} (\partial \dot{v}_r / \partial v_\theta) - \lambda_{v\theta} (\partial \dot{v}_\theta / \partial v_\theta) - \lambda_{v\phi} (\partial \dot{v}_\phi / \partial v_\theta)] \\ r [-\lambda_{v\phi} T - \lambda_{vr} (\partial \dot{v}_r / \partial v_\phi) - \lambda_{v\theta} (\partial \dot{v}_\theta / \partial v_\phi) - \lambda_{v\phi} (\partial \dot{v}_\phi / \partial v_\phi)] \end{bmatrix} \end{aligned} \quad (45)$$

The MCR-to-ECR transformation is now complete, with the ECR costates described by Eqs. (42) and (45). The reverse ECR-to-MCR transformation is found in the same manner.

To ensure numerical accuracy of this technique, the heliocentric state of the capture spiral at the end of the backward numerical integration in both ECR and MCR frames is stored and compared. Because of accumulated errors in the numerical integration processes for both trajectories, there will be some error in both solutions, but the Mars spiral integrated in the MCR frame will typically have less accumulated error. This is due to the scale issue for the radius state component for the ECR integration, in which the changes in radius during the spirals around Mars are many orders of magnitude smaller than the Earth-to-Mars position magnitude. Therefore, the MCR spiral is considered to be the standard, and, ideally, the equivalent ECR trajectory found through the preceding transformation process should match as closely as possible. For shorter Mars spirals, the two trajectories match in heliocentric coordinates to the submeter level, and as the trajectories grow in length and complexity, the error grows. Full round-trip missions found in steps 5 and 6 will typically converge as long as this error remains less than a kilometer in magnitude. When it grows beyond this, convergence is difficult to achieve due to the large error accumulation for the boundary-value solver. Plus, the error then grows too large to be acceptable from a mission design standpoint. A more detailed discussion of these issues can be seen in [4].

#### Step 5

Four steps form the building blocks necessary to solve the full LEO–LMO missions solely in the ECR frame. For the unconstrained VSI case, there are 12 unknowns and 12 constraints in the multiple-shooting problem. The initial and final spherical angles of the spacecraft with respect to Earth and Mars are considered to be fixed, as numerical sensitivity issues arise if these angles are free parameters. Additionally, as shown in [4], once solutions require roughly five revolutions or more to complete the spirals, the performance is very weakly affected by varying the initial or final spherical angles from 0–360 deg. The initial guess of six of the unknown costates comes from the converged solution of step 3a and they are the costates at the initial time. The last six are the values returned from the transformation of the converged MCR costates of step 3b into their equivalent ECR costates at the final time. The 12 constraints correspond to continuity of the six state variables and six costate variables at the patch point at which the forward and backward solutions meet. The time of flight is considered to be fixed, due to the dynamics of a VSI engine that would optimally increase time to infinity. Whereas previous works [5,6] integrated the equations of motion and evaluated the constraints in astronomical canonical units, this work instead uses metric measurements for the integration and percent errors for the constraint evaluations.

The effects of the numerical integration error for the ECR Mars spiral discussed in step 4 could be minimized by applying the transformation at the patch point after integrating the Mars spiral in the MCR coordinates. However, this approach was not used in this research to see the limits of integrating solely in the ECR frame, but for future studies such as LEO-to-LLO missions, this process may be adapted.

#### Step 6

With the reality that numerically exact convergence is not likely for step 5, due to the complexity of the problem and computer-imposed numerical limitations such as numerical integration errors, the solution is refined one last step. Step 6 reduces the number of unknowns and constraints to six and uses just a single-shooting method for fine-tuning step 5. The backward spiral solution is removed and the six departure costates at  $t_0$  from step 5 are run continuously to  $t_f$  at LMO with no patch point. The six targets are the six final state variables of the spacecraft at LMO.

#### $I_{sp}$ Constraints

The preceding six-step process is designed for unconstrained VSI engines in which the vehicle mass and power are decoupled from the problem via Eq. (16). To directly compare with published research

[6],  $I_{sp}$  constraints had to be considered, especially during the Earth escape. To accommodate such constraints, the costates from the unconstrained case are converted to the equivalent costates for a particular vehicle mass and power and the appropriate control limits are then added [3]. The  $I_{sp}$  is constrained to be constant during the escape spirals, and when the spacecraft enters heliocentric space, the engine is allowed to vary between some minimum and maximum  $I_{sp}$  value. For the Mars captures, estimates need to be made for the final mass and mass costate to run the Mars capture spirals backward for step 5, adding two unknowns and two constraints to the boundary-value problem. Although these new unknowns add some complexity to the problem compared with the unconstrained cases, these solutions are still easier to converge than the unconstrained VSI cases. The easier convergence behavior is due to the removal of the high-frequency oscillation of the acceleration magnitude (and  $I_{sp}$ ) seen in the unconstrained cases during the Earth spiral. However, if strict upper  $I_{sp}$  bounds are added to the problem, coast arcs could result, although no solutions are presented with the bounds that are active in these results. These bounds could be easily added as per [2,3], but convergence may be difficult. It should also be noted that if the problem was even further constrained to have a constant specific impulse and allow coast arcs during the spirals, the solutions would be more complex, as the bang–bang control structure would most likely indicate numerous coast arcs that would make convergence difficult.

### Sample Mission Scenarios

The sample missions presented are used as a direct comparison with previously published works [5,6]. Once the programs have been coded with each of the necessary steps, to construct these missions from scratch (starting at steps 1a and 1b) takes roughly three actual hours of user time to find a converged solution for steps 5 and 6. The large part of the effort is spent in the first two steps, creating the families of spirals used to curve-fit the escape and capture spirals. Once this initial ground work is accomplished, finding solutions slightly perturbed from the nominal solution takes a matter of minutes of user time to reconverge steps 3–6.

The epoch used from the JPL DE405 ephemeris to define the two-body orbits of Earth and Mars is 1 February 2014 and the time of flight is fixed at 145 days. The initial orbit of the spacecraft around Earth is at an altitude of 1200 km and has no inclination with respect to the Earth ecliptic plane. Inclined solutions are presented later. The final orbit at Mars is set to be a circular orbit at 6  $DU_M$  and has no inclination with respect to the Mars ecliptic plane. The exhaust engine power is considered to be 6 MW and the initial mass is set at 525,000 kg. For initial guesses for the Earth escape and Mars capture spirals, spirals of 24 and 2 days, respectively, were used for steps 1 and 2. The  $I_{sp}$  is constrained to be 1000 s during the Earth escape and then is permitted to vary above 1000 s for the rest of the trajectory.

For the constrained mission, the final mass upon insertion to a circular orbit at 6  $DU_M$  was 108,895 kg. The final mass for the same mission run in previously published research [6] was 99,316 kg, and so the new trajectory saves 9579 kg of fuel in comparison, which is a significant improvement (9.6% more mass delivered). One reason for the large improvement is explained by the fact that there are numerous local optimal solutions that exist for the escape and capture sequences, as demonstrated for the two-dimensional LEO–LMO missions [4]. The local optimal solution found depends on multiple factors; most important, it depends on the process used to generate the initial estimate of the optimal capture spiral. As discussed in the research [4] on two-dimensional LEO–LMO transfers, better locally optimal spiral escape and capture times exist that provide the best fuel performance in comparison with other escape and capture times. The solution process will yield a local optimal solution that takes approximately the same amount of time and number of revolutions until the spacecraft achieves zero energy with respect to the target planet as the initial guess requires. This then requires the analyst to run a spectrum of guesses for the optimal escape and capture times to find the best local optimal solution.

However, the main reason for the large increased performance in this case is the solution process itself. The process used in the other research [5,6] uses a forward targeting and iterative process that targets very large Martian orbits and iteratively reduces the Martian orbit size with a succession of optimal control problems. This is in contrast to directly estimating the capture sequence with a backward integration from the target LMO orbit that explicitly involves a spiral trajectory. The old process may have the freedom to find a more fuel-optimal nontraditional capture, but it also may find local optimal solutions that may be significantly more fuel-intensive than the traditional spiral capture sequence. This is most likely the case in this example, as the capture sequence presented in the previous work [6] is not a spiral. A spiral capture is expected, based on the results of the two-dimensional solutions [4,5], but this nontraditional capture has an almost 180 deg midcapture reversal of the trajectory, which probably accounts for most of the fuel penalty compared with the new solution. A close-up of the Earth escape is in Fig. 3, and the traditional spiral capture to 6  $DU_M$  is in Fig. 4.

Lower spiral captures at Mars are presented later. The  $I_{sp}$  control history for the constrained case is shown in Fig. 5. The constrained case greatly simplifies the control history during the escape portion of the mission, as seen in Fig. 5, allowing a broader range of solutions in comparison with the unconstrained case, as discussed later. It is important to note the kink in the  $I_{sp}$  history in Fig. 5, which corresponds to the point at which the trajectory leaves the lower  $I_{sp}$  bound. It is not a smooth transition, due to the fact that the  $I_{sp}$  wants to follow its optimal value during the escape, but is constrained to be 1000 s, and the kink is the first point at which the upper bound on the  $I_{sp}$  is removed. In fact, the  $I_{sp}$  is not explicitly required to be continuous in this formulation, but for all examples presented, it is continuous.

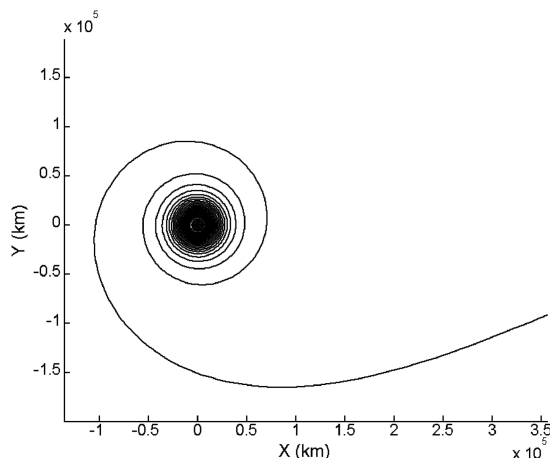


Fig. 3 ECR Earth escape trajectory at  $I_{sp} = 1000$  s during escape.

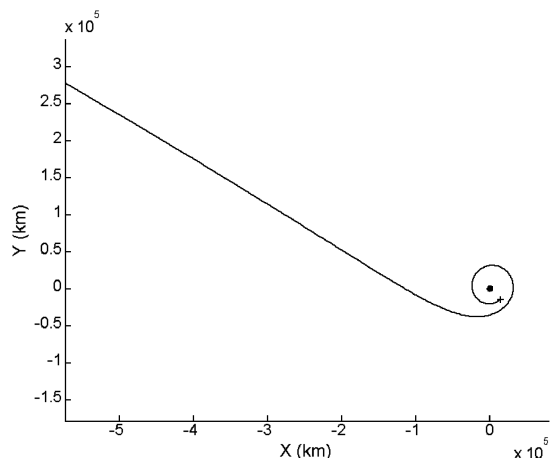


Fig. 4 MCR Mars capture trajectory.

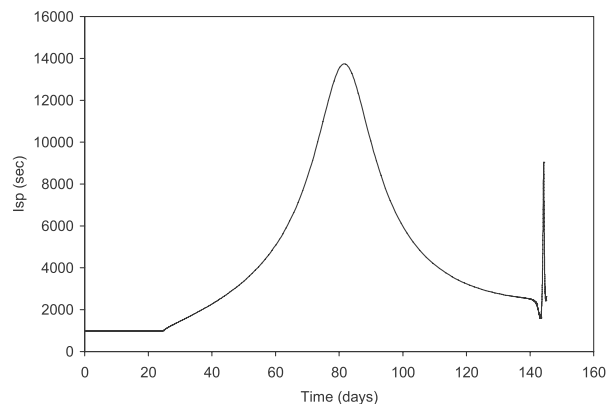


Fig. 5  $I_{sp}$  vs time (constrained case).

#### Finding the Best Local Solutions as Functions of Escape and Capture Times

In addition to the method in Fig. 2 finding better local optimal solutions by initially estimating and setting the structure of the spiral capture sequence, it also allows missions to be found for much lower orbits than the 6  $DU_M$  that were numerically achievable previously. Using this methodology for the unconstrained missions, 2  $DU_M$  (6794 km) circular Martian orbits are achieved. The final mass for the unconstrained mission to 2  $DU_M$  is 105,683 kg, and the final mass for the constrained 1000 s escape is 100,403 kg, a fuel penalty of 5280 kg. For the capture sequence to 2  $DU_M$ , the optimal capture time was found to be 5 days and the optimal escape time was found to be 17 days. The  $I_{sp}$  control history is shown in Fig. 6 for the unconstrained case, and the more detailed  $I_{sp}$  history for the escape is clearly evident.

The optimal value of 17 days for the Earth escape was found by optimizing a range of missions with various initial guesses for the Earth escape time. The process was presented in the two-dimensional case for the Mars capture sequences [4]. As found in that work, the best local optimal  $I_{sp}$  history for an escape or capture in the three-dimensional case has roughly a constant mean value during the high-frequency oscillation seen during the spiral portions of the missions, as shown in Fig. 7. Less fuel-efficient local optimal solutions have the mean value of the  $I_{sp}$  grow for spirals that are too short, as shown in Fig. 8, and the mean  $I_{sp}$  decays for spirals that are too long, as shown in Fig. 9. The decaying and growth behavior is reversed for the Mars capture sequences [4].

For the unconstrained missions, 2  $DU_M$  (6794 km) was the lowest numerically achievable LMO orbit. However, for the constrained missions, lower orbits were achieved. Final orbits of 1.47  $DU_M$  (5000 km) were achieved for missions with the constant- $I_{sp}$  (1000 s) escapes, followed by a variable- $I_{sp}$  profile with the rest of the way. The capture sequence to 1.47  $DU_M$  is shown in Fig. 10, and the  $I_{sp}$  history for the capture sequence is shown in Figs. 11 and 12. The optimal

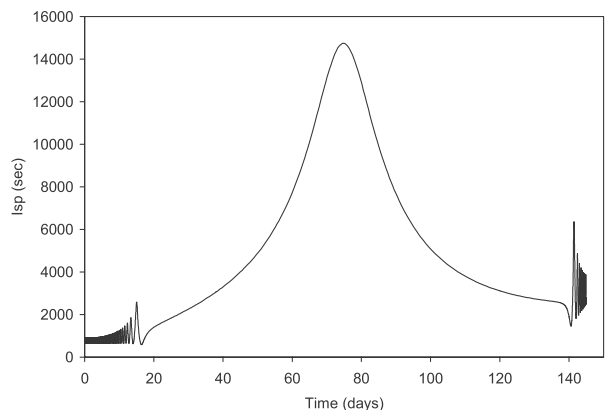


Fig. 6  $I_{sp}$  vs time LEO-LMO (7578 to 6794 km) at  $DE = 17$  days and  $DM = 5$  days.

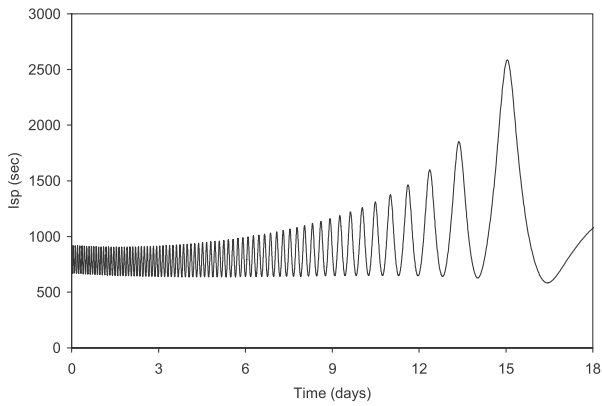


Fig. 7  $I_{sp}$  vs time during Earth escape at  $DE = 17$  days.

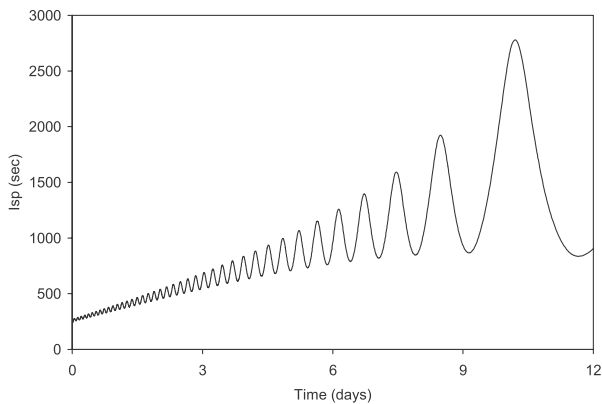


Fig. 8  $I_{sp}$  vs time during Earth escape at  $DE = 10$  days.

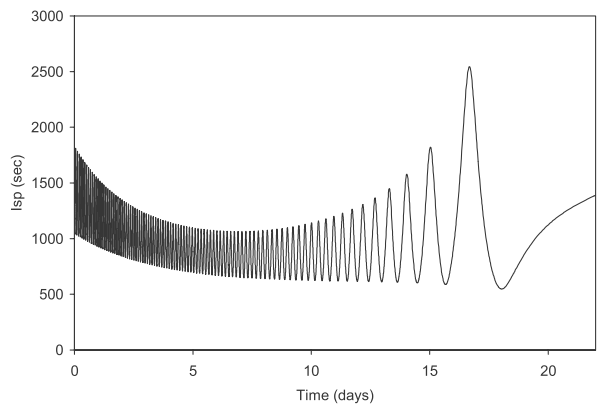


Fig. 9  $I_{sp}$  vs time during Earth escape at  $DE = 24$  days.

capture time to  $1.47 DU_M$  is found to be 5.5 days, with a final mass of 97,330 kg.

The optimal thrust pointing history is shown in Fig. 13, which shows the in- and out-of-plane thrust angles in an ECR frame for the first 139 days of the mission, and Fig. 14, which shows the same thrust angles in an MCR frame for the last 6 days of the trajectory.

### Inclined Capture Orbits

Although these solutions do span three dimensions, as the orbit of Mars is inclined from the orbit of Earth around the sun, all the solutions presented thus far are almost planar. The escape and capture spirals occur mostly in the ecliptic planes of the spiral planets. However, target orbits inclined from these planetary ecliptic frames might be desirable for scientific/mission objectives. The spherical equations of motion do have a singularity for a value of

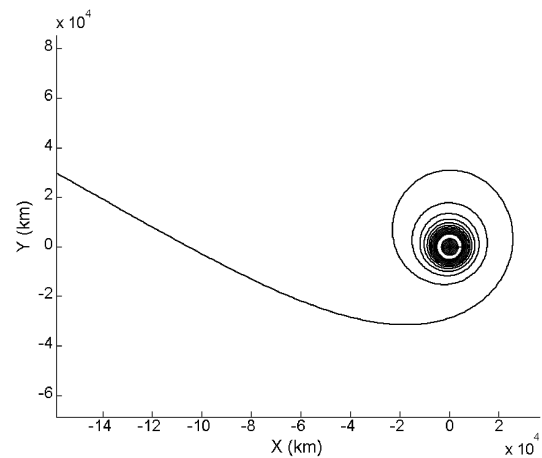


Fig. 10 MCR capture sequence to  $1.47 DU_M$  (5000 km) at  $DM = 5.5$  days.

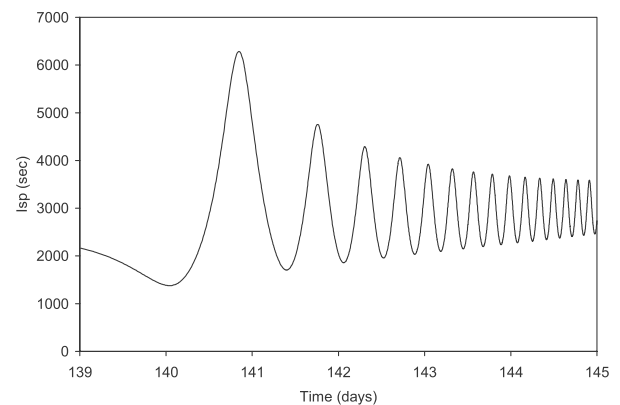


Fig. 11  $I_{sp}$  vs time at  $LMO = 1.47 DU_M$  (5000 km) and  $DT = [139-145]$  days.

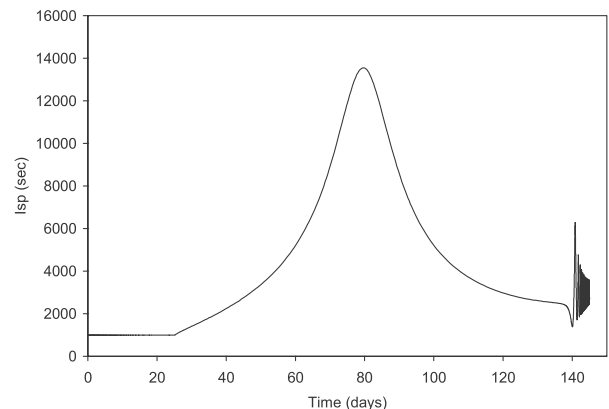


Fig. 12  $I_{sp}$  vs time at  $LMO = 1.47 DU_M$  (5000 km) and  $DT = [0-145]$  days.

$\varphi = 90$  deg, and so examples are presented near this singularity. Mars capture orbits with an inclination of 88 deg are targeted, which are also presented in previous works [6]. For a capture to a  $6 DU_M$  circular orbit inclined at 88 deg from the Mars ecliptic, a final mass of 104,982 kg was found. Previous work found a 103,574 kg final mass [6]. The fuel usage found with the two methods is much closer here than in the noninclined cases. This is most likely due to the fact that for the inclined captures presented in [6], the inclined capture sequence is a more traditional spiral trajectory with no large, abrupt changes of direction. This is more fuel-efficient than the nontraditional capture found in the noninclined case. An oblique



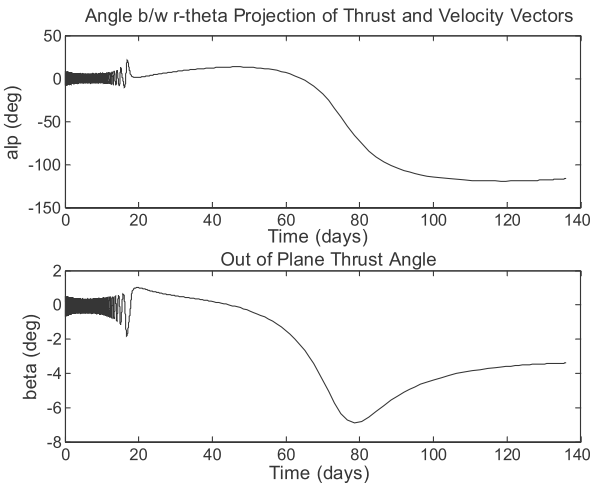


Fig. 13 ECR thrust angle control history  $DT = [0\text{--}139]$  days.

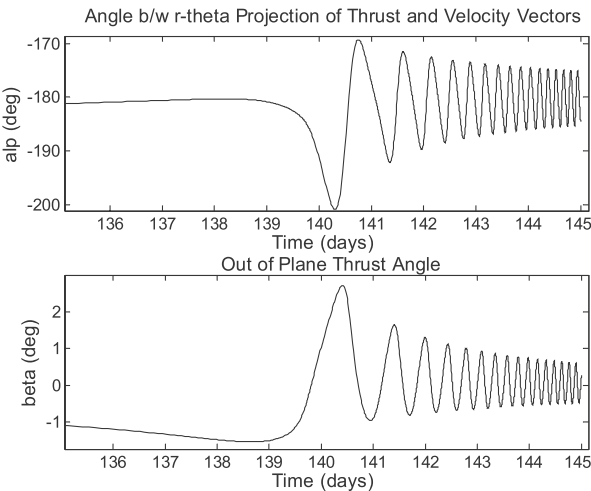


Fig. 14 MCR thrust angle control history, including  $M = 0$  deg and  $DT = [135\text{--}145]$  days.

view of the spiral capture to the inclined 88 deg,  $6\text{ }DU_M$  Martian orbit is shown in Fig. 15.

As with the noninclined cases, this new methodology and the new derivations that allow the entire trajectory to be run in the ECR frame allow much lower orbits to be found than have been published previously. Figure 16 shows an oblique view of the capture to a  $1.47\text{ }DU_M$  (5000 km) orbit at Mars, inclined 88 deg from the Martian ecliptic. The final mass for this mission was 96,483 kg, which is an 847 kg penalty compared with the noninclined solution.

Including Lunar Gravity in LEO-to-LMO Missions

Although the solutions presented thus far use a gravity field in three dimensions that has the Earth, sun, and Mars gravitating at all times, the largest perturbations during the Earth escape come from the moon. In this section, the moon’s effect on the trajectory is included and the missions of the previous sections are recreated. LEO-to-LMO spiral-to-spiral missions that include lunar gravity have not been previously solved as a single-optimization problem. Recall that for these calculations, the planets’ motions are governed

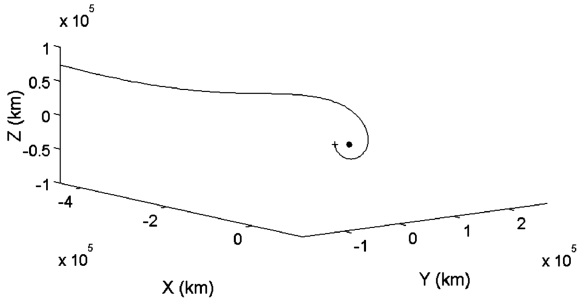


Fig. 15 Oblique view:  $6\text{ }DU_M$  capture, including  $M = 88$  deg.

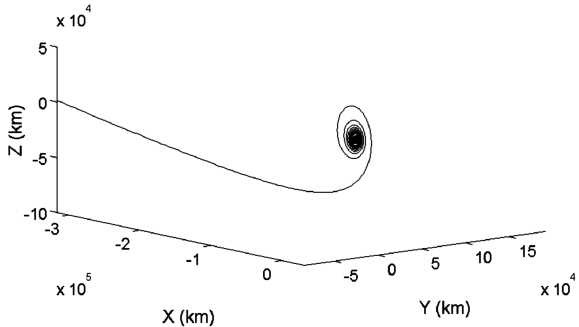


Fig. 16 Oblique view:  $1.47\text{ }DU_M$  capture, including  $M = 88$  deg.

by two-body dynamics based on an epoch from the JPL ephemeris, indicating that each planet moves in just two dimensions with respect to each body’s orbital plane. The motion of the moon is recreated in a similar fashion. The initial state of the moon with respect to the Earth is found from the JPL ephemeris, and then the moon’s motion is integrated based on the two-body dynamics of the moon in orbit around the Earth. The equations of motion and the costate equations must be updated to include the lunar perturbations. They are reformulated based on the moon’s position in heliocentric space, similarly to the procedure used to describe the contributions of Martian gravity on equations of motions referenced to the ECR frame. The updated version of the equations of motion, costate equations, and all other relevant terms are included in [16].

The solution process used to solve the LEO-to-LMO missions with lunar perturbations is identical to the process used in the two- and three-dimensional cases discussed already. However, when calculating the Martian capture sequences for steps 1b–3b in the MCR coordinates, the moon’s gravity is not included, as its effect on trajectories in the close vicinity of Mars is negligible. This allows the original MCR equations of motion and costate equations to not have to be rederived and coded. Initial estimates for the Martian captures are found in the MCR coordinates without lunar gravity and then converted to the ECR coordinates to run the entire trajectory in the ECR frame including lunar gravity.

The impact of including the moon’s gravity on these trajectories without a very close lunar approach is not very significant. These trajectories typically spend less than one lunar cycle in the Earth system before escaping Earth, limiting the moon’s effect. However, including the lunar gravity does make the problem more numerically sensitive, limiting the complexity of the capture sequence at Mars. Captures were only able to be converged for final orbits of 10,000 km or  $2.94\text{ }DU_M$  for both the unconstrained and constrained ( $I_{sp}$  minimum during escape is 1000 s) engine scenarios, compared with

Table 1 Final masses and fuel savings for  $2.94\text{ }DU_M$  capture with and without the moon on a launch date of 1 February 2014

$I_{sp}$ model	$m_f$	No-moon solution	Fuel savings with moon
Unconstrained	109,186.5 kg	109,160.8 kg	25.7 kg
Constrained ( $I_{sp}$ min = 1000 s)	103,881.9 kg	103,926.9 kg	−45 kg

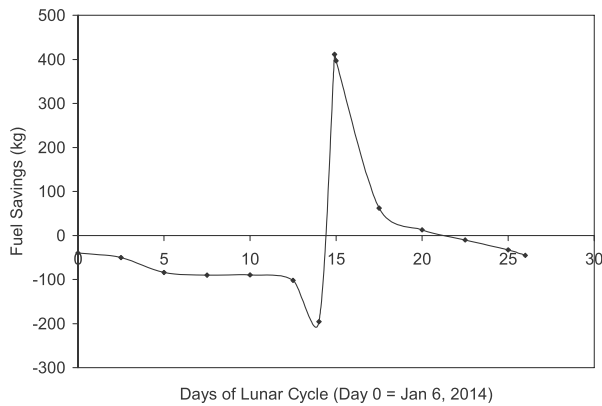


**Fig. 17 Lunar flyby fuel savings compared with the no-moon case vs launch date.**

the achievable limits of 2 and  $1.47 DU_M$ , respectively, without the moon. The fuel performance of solutions with and without the lunar gravity for captures to  $2.94 DU_M$  are seen in Table 1, which shows that the fuel savings when including the moon for the nominal start date is small ( $-45$  to  $+25$  kg).

However, that particular start date does not provide a close encounter with the moon when the spacecraft leaves the vicinity of the Earth. A parametric scan of possible launch dates covering a full lunar cycle was examined to determine if a close lunar flyby during the escape has a more significant impact on the fuel performance. The results of such a scan starting on 6 January 2014 show that if the departure vector from the Earth system does cross the lunar orbit when the moon is in that vicinity, the fuel performance compared with trajectories optimized without lunar gravity is more significantly affected. This behavior is seen in Fig. 17, in which the closest encounter occurs at approximately the 15th day of the lunar cycle (20 January 2014). However, in attempting to find converged solutions for an initial epoch after 20 January but before 21 January proved futile, as the numerical sensitivity of flying that close to the moon combined with all the other aspects of the problem prevented convergence. But the figure clearly shows that immediately before closest lunar approach (the spacecraft crosses ahead of the moon), the fuel performance drops off steeply. The performance increases if the flyby occurs after closest approach with the spacecraft trailing the moon.

The closest lunar approach for a converged trajectory was a relatively large distance of 52,642 km from the moon's center. For these flybys, it must be considered that the spacecraft's escape trajectory takes place mostly in the Earth ecliptic frame, which is inclined from the lunar orbit frame. More significant flybys could occur if the spacecraft's trajectory is explicitly directed out of the Earth ecliptic frame for a closer lunar flyby, but such scenarios were not considered. However, as shown by the inability to converge trajectories for the closest noncoplanar approach shown in Fig. 17 between 20 January and 21 January 2014, having a closer lunar flyby with the spacecraft passing much nearer to the lunar orbital frame and still incorporating the Earth escape and Mars capture spirals is not likely to converge using current techniques. Additionally, the solution process developed thus far would have to be significantly altered to force such a close encounter. Most likely, a third shot would have to be added to the multiple-shooting process of step 5 to enforce the close flyby.

## Conclusions

A step-by-step process is detailed that allows the user to efficiently find fuel-optimal solutions using indirect optimization for interplanetary missions such as a mission for low Earth orbit (LEO) to low Martian orbit (LMO) in three dimensions. This process is based on the two-dimensional model and can accommodate solutions in which the vehicle  $I_{sp}$  is either unconstrained or constrained. The solutions found show a significant improvement in

fuel usage (9.6% more final mass) compared with the published benchmarks. Additionally, more complicated capture sequences were generated with final orbits from 1.47 to 2 Mars radii (5000–6794 km) compared with the previous benchmark of 6 Mars radii (20,382 km) for both planar and highly inclined capture spirals. These spirals were the lowest spirals that were able to be converged and may indicate that this is the numerical/feasible limit of solving such complicated missions via the indirect method.

As in the two-dimensional case, the main difference behind these improvements is the formulation of a multiple-shooting problem in a single Earth-referenced coordinate frame. The use of a single coordinate frame avoids the difficult optimality conditions associated with switching coordinate frames that were required for previous attempts at this problem that used multiple frames. This is made possible by the derivation of a transformation that converts the costates in the Mars-referenced MCR frame and converts them to their equivalent values in the Earth-referenced ECR frame. This then allows a good estimate of a backward capture spiral to be used within the framework of the indirect method, setting up a multiple-shooting problem. The multiple-shooting method inputs accurate initial guesses for both the Earth escape and Mars capture spirals. Previous work used a single-shooting method that only started with an Earth spiral and encountered difficulty in generating the expected structure of the Martian capture sequence.

The trends identified in the two-dimensional case were seen again in three dimensions. In particular, the process demonstrated again that the solution space is filled with local optimal solutions, particularly linked to the initial guess used for the escape and capture times, and that the best locally optimal thrust/ $I_{sp}$  history with respect to the escape/capture times is visually distinct from the nearby local optimal solutions. Additionally, it is shown again that the constraint on the  $I_{sp}$  that simplifies the control history during the complicated Earth escape allows a broader range of missions to converge when compared with unconstrained mission scenarios. The final results presented include lunar gravity during the entire trajectory, which makes a more realistic gravity model but reduces the achievable set of capture scenarios by adding to the numerical complexity of the problem. For the solutions converged including the moon, the moon's gravity mostly imposes a slight fuel penalty, except for missions in which there is a close lunar swingby of the spacecraft's departure vector from the Earth. This swingby imposes a larger change in fuel performance, positive or negative, depending on if the spacecraft passes ahead of or behind the moon.

Future work will apply these techniques to gravity-assist missions and LEO–LLO missions and possibly solving constant-thrust spirals with a bang–bang control history with coast arcs.

## Acknowledgments

The authors would like to express thanks for the support and funding for this research provided in part by the National Science Foundation Fellowship, the Thrust 2000 University of Texas Fellowship, and NASA grant NAG9-1441.

## References

- [1] Ranieri, C. L., and Ocampo, C. A., "Optimization of Roundtrip, Time-Constrained, Finite Burn Trajectories via an Indirect Method," *Journal of Guidance, Control, and Dynamics*, Vol. 28, No. 2, Mar.–Apr. 2005, pp. 306–314.  
doi:10.2514/1.5540
- [2] Ranieri, C. L., and Ocampo, C. A., "Optimizing Finite-Burn, Round-Trip Trajectories with  $I_{sp}$  Constraints and Mass Discontinuities," *Journal of Guidance, Control, and Dynamics*, Vol. 28, No. 4, July–Aug. 2005, pp. 775–781.  
doi:10.2514/1.9188
- [3] Ranieri, C. L., and Ocampo, C. A., "Indirect Optimization of Spiral Trajectories," *Journal of Guidance, Control, and Dynamics*, Vol. 29, No. 6, Nov–Dec 2006, pp. 1360–1366.  
doi:10.2514/1.19539
- [4] Ranieri, C. L., and Ocampo, C. A., "Indirect Optimization of Two Dimensional Finite-Burning Interplanetary Transfers Including Spiral Dynamics," *Journal of Guidance, Control, and Dynamics*, Vol. 31,

- No. 3, May–June 2008, pp. 720–728.  
doi:10.2514/1.30833
- [5] Vadali, S. R., Nah, R., Braden, E., and Johnson, I. L., Jr., “Fuel-Optimal Planar Earth–Mars Trajectories Using Low-Thrust Exhaust Modulated Propulsion,” *Journal of Guidance, Control, and Dynamics*, Vol. 23, No. 3, May–June 2000, pp. 476–482.  
doi:10.2514/2.4553
- [6] Nah, R. S., Vadali, S. R., and Braden, E., “Fuel-Optimal, Low-Thrust, Three-Dimensional Earth–Mars Trajectories,” *Journal of Guidance, Control, and Dynamics*, Vol. 26, No. 6, Nov.–Dec. 2001, pp. 1100–1107.
- [7] Pierson, B. L., and Kluever, C. A., “Three-Stage Approach to Optimal Low-Thrust Earth–Moon Trajectories,” *Journal of Guidance, Control, and Dynamics*, Vol. 17, No. 6, Nov.–Dec. 1994, pp. 1275–1282.  
doi:10.2514/3.21344
- [8] Kluever, C. A., and Pierson, B. L., “Optimal Low-Thrust Three Dimensional Earth–Moon Trajectories,” *Journal of Guidance, Control, and Dynamics*, Vol. 18, No. 4, July–Aug. 1995, pp. 830–837.  
doi:10.2514/3.21466
- [9] Kluever, C. A., and Pierson, B. L., “Optimal Low-Thrust Earth–Moon Trajectories Using Nuclear Electric Propulsion,” *Journal of Guidance, Control, and Dynamics*, Vol. 20, No. 2, Mar.–Apr. 1997, pp. 239–245.  
doi:10.2514/2.4058
- [10] Guelman, M., “Earth-to-Moon Transfer with a Limited Power Engine,” *Journal of Guidance, Control, and Dynamics*, Vol. 18, No. 5, Sept.–Oct. 1995, pp. 1133–1138.  
doi:10.2514/3.21515
- [11] Sakai, T., and Olds, J., “Development Of A Multipurpose Low Thrust Interplanetary Trajectory Calculation Code,” *Advances in the Astronautical Sciences*, Vol. 116, No. 3, 2004, pp. 2597–2612
- [12] Sakai, T., Olds, J., and Alemany, K., “Development of SAMURAI-Simulation and Animation Model Used for Rockets with Adjustable  $I_{sp}$ ,” *Advances in the Astronautical Sciences*, Vol. 120, No. 2, 2005, pp. 1297–1316
- [13] Sauer, C. G., Jr., “Optimization of Multiple Target Electric Propulsion Trajectories,” 11th AIAA Aerospace Sciences Meeting, AIAA, Washington, D.C., AIAA Paper 73-205, Jan. 1973.
- [14] Hull, D. G., *Optimal Control Theory for Applications*, Springer, New York, 2003, pp. 276–316.
- [15] Lawden, D. F., *Optimal Trajectories for Space Navigation*, Butterworths, London, 1963, pp. 79–94.
- [16] Ranieri, C. L., “Indirect Optimization of Interplanetary Trajectories Including Spiral Dynamics,” Ph.D. Dissertation, Univ. of Texas at Austin, Austin, TX, 2007.